



On flow structures associated with large wall mass transfer coefficients in orifice flows



Feng Shan^{a,*}, Zhichun Liu^a, Wei Liu^a, Yoshiyuki Tsuji^b

^a School of Energy and Power Engineering, Huazhong University of Science and Technology, Wuhan 430074, PR China

^b Department of Energy Engineering and Science, Nagoya University, Nagoya 464-8603, Japan

ARTICLE INFO

Article history:

Received 15 December 2015

Received in revised form 25 May 2016

Accepted 5 June 2016

Available online 15 June 2016

Keywords:

Orifice flow

Stochastic estimation

Wall mass transfer coefficient

Coherent structures

ABSTRACT

In this study, the turbulent flow field is simultaneously measured by stereoscopic particle image velocimetry (SPIV) and the wall mass transfer coefficient using the limiting diffusion current technique (LDCT). SPIV measurements of the flow field behind an orifice in a round pipe are performed in the cross and longitudinal sections. One-point linear and quadratic stochastic estimations are employed to calculate the conditional average of the flow field associated with the large wall mass transfer coefficient. The results suggest that the counter-rotating vortex pairs play an important role in the large wall mass transfer coefficient. The flow structures associated with a large wall mass transfer coefficient in the cross sections are found to be similar to the flow structures enhancing the wall heat transfer obtained by a theoretical analysis and numerical study in literature.

© 2016 Elsevier Ltd. All rights reserved.

1. Introduction

The heat and mass transfer behind orifices is of considerable theoretical and engineering importance, as this phenomenon appears widely in a variety of engineering applications. Consider, for example, the problem of pipe walls thinning in nuclear/fossil power plant pipelines. Such wall thinning is mainly caused by flow-accelerated corrosion (FAC), which is common in carbon steel pipes, where the wall's iron ions diffuse into the turbulent bulk flow through the oxide layer coating the wall's surface [1]. Although FAC is affected by many factors—such as flow field, water chemistry, and temperature—the rate at which walls thin in nuclear/fossil power plant pipelines is generally considered to be the result of a mass transfer phenomenon driven by the concentration gradient of the iron ions on wall surfaces and in the bulk flow [1]. Indeed, a popular area of study within FAC research is determining what kinds of flow structures enhance the mass transfer coefficient at the wall (hereafter referred to as the “wall mass transfer coefficient”). However, this topic involves a basic and difficult problem—that is, the necessity of simultaneously measuring the concentration field (or, equivalently, the wall mass transfer coefficient) and the velocity field in wall-bounded flows.

The present paper focuses on flow structures associated with large wall mass transfer coefficients at high Schmidt numbers (lar-

ger than 1000) behind circular orifices in round pipes. Our study is conducted in relation to an actual instance of pipe-wall thinning that caused a very serious accident at the Japanese Mihama Nuclear Power Plant in 2004 [2]. Although this study only deals with mass transfer, it is possible to use the Chilton–Colburn analogy to consider a relation between wall mass transfer and wall heat transfer; thus, this study could also be of some value when discussing structures associated with wall heat transfer.

Orifice flow is a typical, separated, internal flow that includes extremely complex flow separation, reattachment, and redevelopment processes. A separated internal flow may be encountered in many practical situations—such as in the immediate vicinity of valves, orifices, nozzles, and boiler tube gags as well as in sudden changes of the pipeline diameter, and it may also exist in the region adjacent to electrochemical cell inlet ports. Hence, it is widely believed that the characteristics of flow structures associated with large wall mass transfer coefficient should exist in many flow fields. Previous research relating to the characteristics of heat/mass transfer in separated internal flows has mainly concentrated on two findings: the peaked, streamwise distribution of heat/mass transfers downstream of sudden pipe changes and the empirical relation between the peak heat/mass transfer values, the Reynolds number, and the Prandtl/Schmidt number [3–5].

With the development of supercomputers, a number of numerical simulations of turbulent mass transfers at solid boundaries have been reported in recent years [6–9]; there is a comparative lack of experimental research regarding turbulent mass transfers

* Corresponding author.

E-mail address: shanfeng@hust.edu.cn (F. Shan).

at solid walls—particularly in the case of separated internal flows. For example, Yamagata et al. have measured the wall mass transfer coefficient behind an orifice in a circular pipe using the benzoic acid dissolution method in a water flow [10]—a method that allowed them to measure the mass transfer at the Schmidt number under conditions that were similar to the actual operating conditions of the pipeline. Their results indicate that, because of flow turbulence, the Sherwood number behind the orifice reaches its maximum value within an area of 1–2 pipe diameters from the orifice; that value then decreases gradually downstream. This trend agrees qualitatively with the features of pipe-wall thinning data; moreover, although their Schmidt number greatly differs from the value we obtain in our mass transfer study wherein the electrochemical method is used [11], the distribution of the wall mass transfer coefficient agrees qualitatively well. The different orifice to pipe diameter ratios (β ratios) and the thicknesses of orifice plates are believed to be responsible for the discrepancies. Utanohara et al. report that the profile of the measured FAC rate can be well correlated with the profile of the root mean square of the wall shear stress, as was predicted by LES [12]; their flow field results, as predicted by RANS and LES, were validated by their LDV data.

Furthermore, some researchers have used the naphthalene sublimation method to measure the wall mass transfer coefficient of flows behind orifices and have discussed the mechanism involved in asymmetric pipe-wall thinning in relation to the combined effect of swirling flow and orifice bias [13,14]. In this respect, the naphthalene sublimation method allows the measurements of mass transfer coefficients in air flows at low Schmidt numbers. In addition, some researchers have studied the effects of swirling flow on mass and momentum transfers downstream of a pipe with elbow and orifice [15]. More specifically, they have used the plaster dissolution method to measure the distribution of the wall mass transfer coefficient downstream of the orifice and have explained why the pipe-wall thinning rate is not uniformly distributed when there is swirling flow upstream of the orifice plate [15]. This nonuniform distribution of pipe-wall thickness in the circumferential direction of the pipe greatly accelerates pipe breakdowns in the industry. In addition, proper orthogonal decomposition (POD) has been applied to analyze the large-scale energetic turbulent structures responsible for nonuniform thicknesses within pipe walls [16]; such findings greatly contribute to our understanding of the nonuniform distribution evident in the Mihama Nuclear Power Plant pipe that is herein evaluated.

Despite the considerable amount of research conducted, interactions between the underlying flow structures at a solid boundary and the associated turbulent heat/mass transfer are still not well understood because of the various obstacles involved in simultaneously measuring velocity and concentration fields close to a solid boundary. The present study is a continuation of our previous work relating to the characteristics of a flow field [17] and that relating to the relationship between a flow field and mass transfer at a wall [11]. Although we have already shown that a strong relation exists between fluctuations in the wall mass transfer coefficient and velocity components, it is still difficult to say what kind of flow structures are responsible for enhancing the wall mass transfer coefficient just by looking at the contour plot of the spatial–temporal correlation of the wall mass transfer coefficient and the flow field. This objective can be fulfilled by using the conditional average technique. More specifically, we can conditionally average the flow field when the wall mass transfer coefficient is large. However, a conventional conditional average is not practical if we are using the time-resolved PIV measurements, which require huge amounts of computer memory and other computational costs. Fortunately, stochastic estimation is able to calculate the conditional average with much less data. Stochastic estimation is the approximation, or estimation, of a random variable in terms

of other random variables [18]; Adrian first proposed of its application to extract coherent motion in turbulent flows [19]. Since then, it has been widely used in the community of fluid dynamics (for example, [20–22]), where the velocity field or pressure has been mostly used to perform stochastic estimation. Indeed, the accuracy of stochastic estimation has been tested many times in many different flows, always with almost unreasonable success [23]. Therefore, in this study, we use stochastic estimation to estimate the conditional average of the flow field when a very large wall mass transfer coefficient appears; this, thus, enables us to focus on the structures associated with large wall mass transfer coefficients. To the best of our knowledge, this is the first study to use a wall mass transfer coefficient in the stochastic estimation of flow field structures.

2. Experimental setup

The problem of pipe-wall thinning is not directly discussed here; instead, we consider the pipe-wall thinning problem as a wall mass transfer phenomenon in which ferrous ions from the carbon steel wall transfer into the bulk flow. This consideration is consistent with a theoretical consideration that views pipe-wall thinning in relation to corrosion [24]. For this study, LDCT was used to measure the wall mass transfer coefficient. For a detailed discussion of LDCT, please refer to [11] and the references therein. In LDCT, we used a polarized condition wherein an adequately large voltage was applied to an electrochemical cell in which the current was controlled by the rate of the wall mass transfer coefficient and wherein the concentration of the reactant was always zero at the surface of the test electrode. The measured electric current was therefore proportional to the mean rate of the mass transfer over the test electrode.

Fig. 1 shows a sketch of the SPIV in both cross and longitudinal sections. A three-electrode system was employed in the chemical reaction [11], which used a small cathode to measure the local wall mass transfer coefficient, a much larger anode, and a reference electrode. The local electrodes acting as the cathode in the electrochemical reaction are depicted as small yellow dots in Fig. 1; note that, to clarify the test section, only some of the local cathodes are shown in the figure. The cathodes for measuring the local wall mass transfer coefficient are circular and have diameters of 1 mm. The anode is much larger than the local cathode and is a circular ring (with a thickness of 1 cm) mounted flush against the pipe wall, as shown in Fig. 1. In our former study [11], we determined the location of the maximum mean wall mass transfer coefficient to be $x_{\max} \approx 2R$.

We made two types of simultaneous measurements, as indicated by the laser sheet in Fig. 1. Note that, only some laser sheet locations are shown to clarify the figure. We simultaneously measured the flow field in the longitudinal section and the wall mass transfer coefficient at the location of the maximum mean wall mass transfer coefficient x_{\max} ($x/R = 2.0$) just as we did in the previous study [11]. Additionally, we simultaneously measured the flow field and the wall mass transfer coefficient of three cross sections at $x/R = 1.8, 2.0$ and 4.0 , respectively. Therefore, in this study, we discuss flow structures based on both the longitudinal and cross sections, as shown in Fig. 1.

The viscosity of the working fluid was measured by a viscometer, and its density ρ was calculated by the equation $\rho = m/V$, where m and V are the mass and volume of the working fluid, respectively. The Reynolds number based on the pipe's diameter and mean velocity was 25,000, and two temperatures of the working fluid ($T = 283$ K, 298 K) were measured, which correspond to two Schmidt numbers (2770 and 1600). All other experimental conditions were similar to those in our previous study [11].

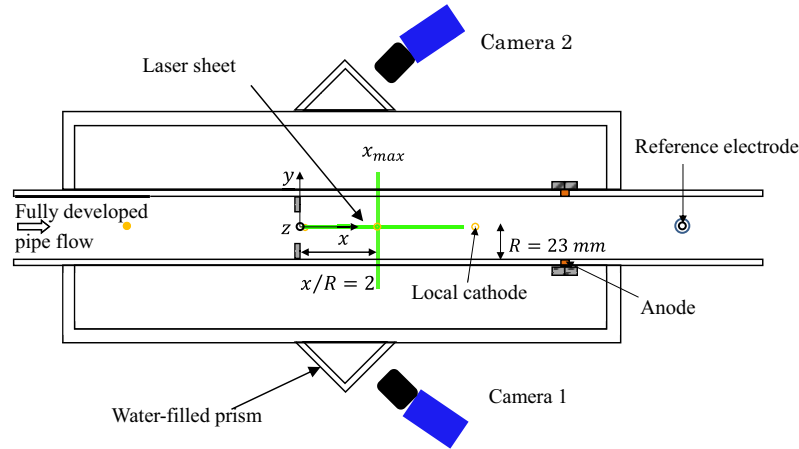


Fig. 1. Sketch of our simultaneous measurements; for clarification, only some of the local cathodes and laser sheet locations are shown.

3. Stochastic estimation of the conditionally average flow field on the basis of the wall mass transfer coefficient

It is usually possible to use conditional average to calculate the turbulent flow field associated with a condition, where the average of the flow field is collected when the fluctuation of the wall mass transfer coefficient satisfies the specified condition. However, stochastic estimation offers a huge advantage over conditional average [25], since calculating the conditional average requires directly finding the realizations of the flow field and the fluctuations of the wall mass transfer coefficient that satisfy the prescribed condition and since it is usually necessary to use immense amounts of data to build up a stable conditional average. In contrast, stochastic estimation requires evaluation of the correlations between the flow field and the fluctuation of the wall mass transfer coefficient, and such correlations are straightforwardly calculated. In the calculation of the two-point correlations between the flow field and the fluctuation of the wall mass transfer coefficient, it is possible to use all data samples instead of selecting only the data samples that satisfy the conditions.

To be specific, we define the largest 20% of all measured coefficients of the wall mass transfer coefficient as the condition of large wall mass transfer coefficient. Therefore, if we use conventional conditional averaging to calculate the velocity field associated with the condition of the large wall mass transfer coefficient condition, only 20% of the measured velocity fields can be used. However, if we use stochastic estimation to calculate the conditional average associated with the condition of the large wall mass transfer coefficient, every measured velocity field can be used since only unconditional cross correlation is needed. In other words, at least five times the number of velocity fields is required for conventional conditional average as for stochastic estimation. For the purposes of the present study, wherein flow field measurements are taken using a high-speed camera, requiring five times more velocity fields creates a much larger burden for cameras and computers and requiring much longer calculation times. Therefore, we used the stochastic estimation method instead of the conventional conditional average technique.

A brief introduction of the equations used in the stochastic estimation of the conditional velocity field in the longitudinal section, based on the condition of the wall mass transfer coefficient, is provided as an example. Since such estimation in the cross section is quite similar to that in the longitudinal section, those equations are not provided here. The velocities and wall mass transfer coefficient in all equations in the present paper present fluctuating com-

ponents. The conditional average can be estimated by a power series, as shown by Guezennec [26].

$$\langle u_{xyi}|k \rangle = A_{xyip}k_p + B_{xyimn}k_m k_n + C_{xyipqr}k_p k_q k_r + \dots \quad (1)$$

where $\langle u_{xyi}|k \rangle$ represents the conditional average of the turbulent flow field u_{xyi} based on the fluctuations of the wall mass transfer coefficient k ; the angle bracket denotes ensemble average; the subscripts x and y denote the position (2D) in the flow field, as shown in Fig. 1; subscript i denotes the velocity components of interest ($i = 1, 2, 3$); subscripts $p, m, n, q,$ and r of the wall mass transfer coefficient k represent different events; and $A_{xyip}, B_{xyimn},$ and C_{xyipqr} represent stochastic estimation coefficients. The stochastic estimation coefficients are found by minimizing the mean square error of the estimate, which depends on where the estimate is truncated [27]. The summation convention is utilized, and the sum is taken from 1 to P , where P is the number of estimating events (in this case, the total number of wall mass transfer measurements). In the present study, the stochastic estimation is formulated using zero time lag correlations; thus, for simplicity, time is dropped when deriving formulations. In addition, we use only one estimating event in the wall mass transfer fluctuations, i.e., $P = 1$. However, different numbers for the terms on the right-hand side of Eq. (1) can be used in the estimation. More specifically, if every term is truncated after the first term on the right-hand side of Eq. (1), this is known as a linear stochastic estimation (LSE); if the first two terms on the right-hand side of Eq. (1) are retained, this is known as a quadratic stochastic estimation (QSE). Usually, terms with orders higher than two have little effect on the accuracy of the estimation; thus, only the LSE and QSE results are discussed in the present study. Below, we present only those equations used to directly calculate the LSE and QSE. For details of their derivation, please see [27].

3.1. Linear stochastic estimation (LSE)

The linear estimate involves only one set of coefficients, i.e., it retains only the first term of Eq. (1):

$$\langle u_{xyi}|k \rangle \approx A_{xyi,\text{lin}}k \quad (2)$$

where $A_{xyi,\text{lin}}$ is the LSE coefficient. In order to distinguish the coefficient used in the LSE from the coefficient used in the first term of QSE, we use $A_{xyi,\text{lin}}$ in the LSE. Using one estimation event, $A_{xyi,\text{lin}}$ is calculated as follows [22]:

$$A_{xyi,\text{lin}} = \frac{\langle u_{xyi}k \rangle}{\langle kk \rangle} \quad (3)$$

where u_{xyi} and k are the same as in Eq. (1) and the angle bracket represents the ensemble average.

To obtain the stochastic estimation of the conditional average of the turbulent flow field for a range of wall mass transfer fluctuation values—e.g., $k > c_0 k_{rms}$ (where c_0 is threshold and k_{rms} is the root mean square of k)— k in Eq. (2) is replaced with the appropriate conditional moment. More specifically, the linear stochastic estimation of the conditional averages of the fluctuations of the wall mass transfer coefficient becomes

$$\langle u_{xyi} | k > c_0 k_{rms} \rangle = A_{xyi,lin} \langle k | k > c_0 k_{rms} \rangle \quad (4)$$

where

$$\langle k | k > c_0 k_{rms} \rangle = \frac{\int_{c_0 k_{rms}}^{\infty} k \cdot \text{pdf}(k) dk}{\int_{c_0 k_{rms}}^{\infty} \text{pdf}(k) dk} \quad (5)$$

and where $\text{pdf}(k)$ is the probability density function of the wall mass transfer coefficient fluctuations.

3.2. Quadratic stochastic estimation (QSE)

The quadratic estimate involves the first two terms of Eq. (1):

$$\langle u_{xyi} | k \rangle = A'_{xyip} k_p + B_{xyimn} k_m k_n \quad (6)$$

In the calculation of the coefficients, the linear and quadratic coefficients are not independent; hence, the coefficients for the linear term in the quadratic estimate are slightly different from the coefficients in the linear estimate. Therefore, we use a prime of the coefficient of the first term in Eq. (6).

The coefficients of the QSE are as follows:

$$[AB]_{xyi} = \begin{bmatrix} A'_{xyi,quad} \\ B_{xyi} \end{bmatrix} = [kk]^{-1} [VK]_{xyi} \quad (7)$$

where the square bracket represents a matrix; $[AB]$ is the matrix composed by the stochastic estimation coefficients A and B ; subscripts x , y , and i are the same as those in Eq. (1); $A'_{xyi,quad}$ is the coefficient of the linear term in the QSE; B_{xyi} is the coefficient of the quadratic term in the QSE; $[VK]_{xyi}$ is a matrix composed by the cross correlation of the velocity field and the wall mass transfer coefficient, as shown in Eq. (8); and $[kk]$ is a matrix composed by moments of wall mass transfer fluctuations, as shown in Eq. (9), where superscript -1 represents the inverse of a matrix

$$[VK]_{xyi} = \begin{bmatrix} \langle u_{xyi} k \rangle \\ \langle u_{xyi} k k \rangle \end{bmatrix} \quad (8)$$

$$[kk]^{-1} = \begin{bmatrix} \langle kk \rangle & \langle kkk \rangle \\ \langle kkk \rangle & \langle kkkk \rangle \end{bmatrix}^{-1} \quad (9)$$

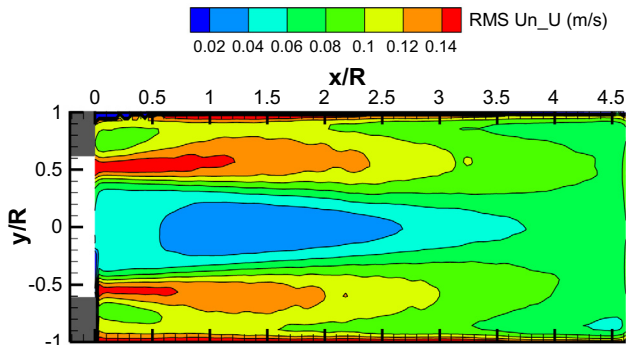


Fig. 2. Root mean square of the uncertainty of the instantaneous streamwise velocity.

Likewise, to obtain the stochastic estimation of the conditional average of velocity fluctuations for a range of wall mass transfer fluctuation values—e.g., $k > c_0 k_{rms}$ —the equations become

$$\langle u_{xyi} | k > c_0 k_{rms} \rangle = A'_{xyi,quad} \langle k | k > c_0 k_{rms} \rangle + B_{xyi} \langle k^2 | k > c_0 k_{rms} \rangle \quad (10)$$

where

$$\langle k^2 | k > c_0 k_{rms} \rangle = \frac{\int_{c_0 k_{rms}}^{\infty} k^2 \cdot \text{pdf}(k) dk}{\int_{c_0 k_{rms}}^{\infty} \text{pdf}(k) dk} \quad (11)$$

4. Results and discussion

4.1. Uncertainty analysis of the experimental results and accuracy of the stochastic estimation

We have already discussed the uncertainty analysis of the wall mass transfer measurement in detail in a previous study [11]. More specifically, we compared our wall mass transfer results in a fully developed pipe flow with a semi-empirical equation proposed in [28] to demonstrate the accuracy of our measurements. Quantification of the PIV uncertainty has rapidly progressed recently [29–31]. Therefore, we very briefly show the PIV uncertainty results using the correlation statistics method embedded in the advanced commercial software package Davis 8.3.0, as proposed by Wieneke [32].

Fig. 2 shows the root mean square of the uncertainty of instantaneous streamwise velocity as an example. It demonstrates that the uncertainty of streamwise velocity is highly dependent on the property of the flow field itself. For instance, in the shear-layer region where the velocity gradient is extremely large, the uncertainty of the flow field is also very large (above 0.1 m/s); however, given the fact that the velocity magnitude is also very large, this large uncertainty is acceptable. In addition, the uncertainty in the region very close to the wall (approximately 0.1 R from the wall) is also very large. Such results are unsurprising since, as is well known, the high-velocity-gradient shear layer and near-wall regions are very challenging for PIV. Meanwhile, the uncertainty in the core region is very small, where the flow is very stable. The uncertainty in other regions ranges from 0.06 m/s (approximately 0.2 pixel/s) to 0.12 m/s (approximately 0.4 pixel/s), which is close to the reported uncertainty range for conventional, double-pulse PIV experimental data. Therefore, we believe that the data in the present study is acceptable. The uncertainty profile of vertical velocity in the longitudinal section is similar to that shown in Fig. 2, only with a lower magnitude. Similar conclusions can be obtained regarding the quantification of the uncertainty in the cross-sectional measurements, which are not shown here for brevity.

The best and most direct method for addressing the accuracy of the LSE and QSE used in the present study is to compare the results obtained by the LSE and QSE with those obtained by conventional conditional averages. However, this is not practical for the present study. The accuracy of stochastic estimation in fluid dynamics has been tested many times in many different flows [23,33]. Therefore, we believe it is reasonable to apply stochastic estimation in the present study. We think that as long as we obtain the convergent cross correlation of the velocity field and the wall mass transfer coefficient, it is possible to obtain accurate stochastic estimation results. From the equations given in Sections 3.1 and 3.2, we can see that we need the convergent cross correlation of $\langle u_{xyi} k \rangle$, $\langle u_{xyi} k k \rangle$, the second-order moment $\langle k k \rangle$, the third-order moment $\langle k k k \rangle$, and the fourth-order moment $\langle k k k k \rangle$ of the wall mass transfer coefficient fluctuations. In this respect, for each loop of the simultaneous measurement, we measured the mass transfer

coefficient for 2 min; the total number of loops for the simultaneous measurements is six in the longitudinal section and eight in the cross section. Therefore, we measured the wall mass transfer for 28 min to guarantee the convergence of the fourth-order moment ($kkkk$). To obtain the convergence of the cross correlation of $\langle u_{xyi}k \rangle$ and $\langle u_{xyi}kk \rangle$, we suppose that if we obtain convergent third-order moments of the velocity fluctuations, then we can obtain the convergent cross correlation of $\langle u_{xyi}k \rangle$ and $\langle u_{xyi}kk \rangle$. Therefore, we compared the third-order moments of velocity fluctuations in the present study with the data we obtained in our previous statistical measurements, which used CCD cameras [17]. A comparison of the two shows reasonable agreement; for brevity, that comparison is not included here.

4.2. Statistical quantity of the flow field in the cross sections

The statistical quantity of the flow field in the longitudinal section behind an orifice in a round pipe has already been presented in our previous studies [11,17]; we therefore only show the statistical quantities of the velocity field in the cross section at $x/R = 2$ as an example. Fig. 3 shows the contours of the mean streamwise velocity and the turbulent kinetic energy. It is possible to clearly observe the axisymmetric property of both mean streamwise velocity and turbulent kinetic energy from Fig. 3. In addition, the statistical quantities agree very well with those from longitudinal measurements presented elsewhere [11,17], which suggests that the PIV measurements taken in the cross sections of the present study are quite accurate.

4.3. Statistics of the wall mass transfer coefficient fluctuations

In this section, we analyze the statistical properties of the wall mass transfer coefficient fluctuations at $x/R = 2$ as an example. Fig. 4 shows the probability density function (pdf) and cumulative distribution function (cdf) of the wall mass transfer fluctuation k at $x/R = 2$ normalized by its root mean square value k_{rms} . The colors of the two y-axis correspond with those of the profiles of the functions. In other words, the black broken line representing the pdf

of k/k_{rms} is described by the left y-axis, and the red solid line representing the cdf of k/k_{rms} is described by the right y-axis. In addition, several thinner dotted lines are used to assist in defining certain quantities. From the profile of the pdf and the vertical dotted line $k/k_{rms} = 0$, it is possible to observe that the fluctuation of the wall mass transfer at $x/R = 2$ deviates from the Gaussian distribution. The horizontal red dotted line in Fig. 4 shows that the cdf of k/k_{max} equals 0.8. We use the values k_{large} to define the region of large wall mass transfer coefficient fluctuations. k_{large} refers to nondimensional values normalized by k_{rms} . In other words, we define 20% of the wall mass transfer fluctuation values ($k/k_{rms} > k_{large}$) as large values. The flow field structures associated with this region is discussed in following sections.

4.4. Single-point stochastic estimation of the flow field

To obtain a stochastic estimation of the flow field on the basis of specified wall mass transfer coefficient conditions, we define the large wall mass transfer coefficient to be the condition at which the fluctuation in the wall mass transfer coefficient is greater than k_{large} , i.e., $k > k_{large}$. All calculations are based on the equations presented in Section 3. Note that, the coefficients for the stochastic estimation (including both the LSE and QSE) are only determined by the statistical properties of the velocity fields and wall mass transfer coefficient time series as well as the unconditional cross-correlation functions between the velocity field and the wall mass transfer coefficient. In other words, the stochastic estimation coefficients are not dependent on the specified conditions, which are determined by the events of interest. The conditional turbulent structures obtained by the stochastic estimation are then determined by both the stochastic estimation coefficients and the specified conditions. In the single-point stochastic estimation in the present study, the wall mass transfer coefficient at one location is the specified condition. From the equations for single-point stochastic estimation in Section 3, we know that the specified condition can only affect the magnitude of the obtained flow structures and cannot change the shape of these structures. That is,

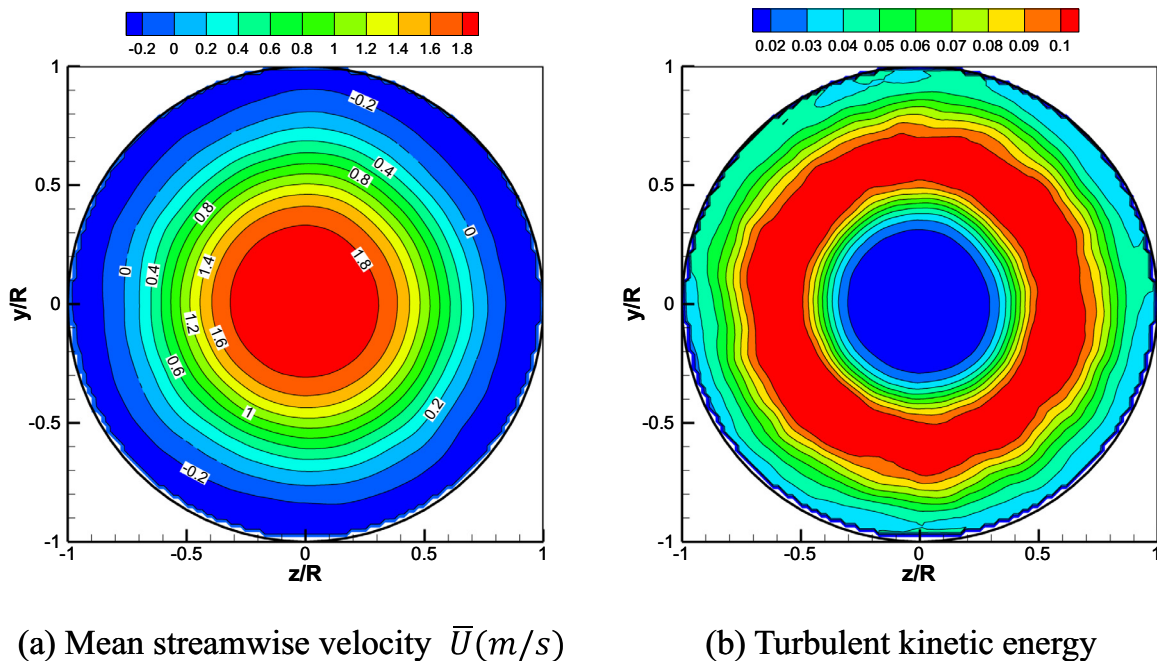


Fig. 3. Contours of the statistical quantities at $x/R = 2$.

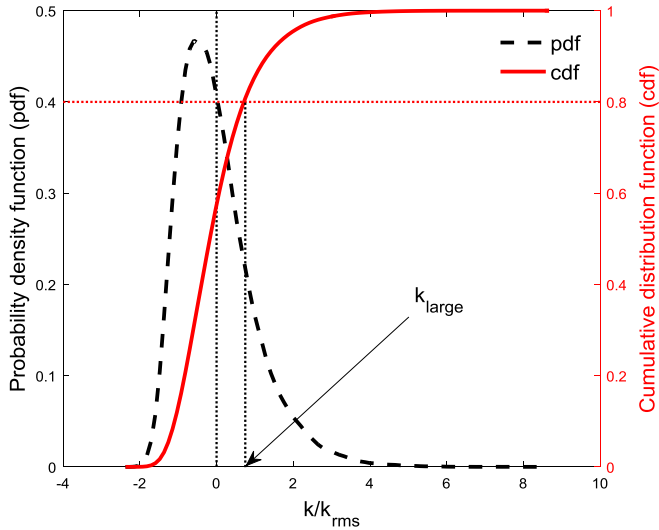


Fig. 4. Probability density function (pdf) and cumulative distribution function (cdf) of the fluctuation in the wall mass transfer coefficient k at $x/R = 2$, normalized by its root mean square, k_{rms} .

the shape of the conditional flow structures obtained in the present study are not dependent on the specified conditions.

After performing a stochastic estimation of the velocity field, the coherent structures are extracted from the velocity gradient tensor, as proposed in [34]. More specifically, the swirling and shear strength b is calculated as follows:

$$b = \frac{\partial u}{\partial y} \cdot \frac{\partial v}{\partial x} - \frac{1}{2} \left(\frac{\partial u}{\partial x} \cdot \frac{\partial v}{\partial y} \right) + \frac{1}{4} \left[\left(\frac{\partial u}{\partial x} \right)^2 + \left(\frac{\partial v}{\partial y} \right)^2 \right] \quad (12)$$

where the pattern is shear when b is negative and is a swirl when b is positive.

Fig. 5 shows nondimensional swirling, shear strength, and streamline patterns based on the LSE and QSE of $\langle u_{xyi} | k > k_{large} \rangle$ in the longitudinal section for both two temperatures of the working fluid. b is normalized by \bar{U}_0^2/D^2 , where U_0 is the mean upstream pipe flow streamwise velocity, and D is the pipe diameter. The arrows at the bottom of the graphs represent the locations of the mass-transfer measurement sensor. The stochastic estimation can be used to calculate both the instantaneous and conditional averages of the flow field. If it is used to estimate the instantaneous flow field on the basis of the wall mass transfer coefficient, it results in large errors as the correlation between the flow field and the wall mass transfer coefficient decays to zero, ultimately approaching the root mean square of the flow field. On the other hand, if the stochastic estimation is used to estimate the conditional average flow field, the error in the stochastic estimation may still be small because the conditional average flow field also vanishes as the correlation between the flow field and the wall mass transfer coefficient decays to zero, e.g., if the flow field is very far from the wall mass transfer measurement sensor [25]. Therefore, the stochastic estimation of the conditional velocity field is only calculated in the region close to the sensor of the wall mass transfer measurement between $0.5 \leq x/R \leq 3.5$ and $-1 \leq y/R \leq 0$, as shown in Fig. 5. From Fig. 5(a) and (c), we can observe that a large wall mass transfer coefficient is associated with two vortex structures (positive contours) on the two sides of the wall mass transfer measurement sensor. Additionally, shear structures (negative contours) can be observed just on the top of the mass transfer measurement sensor in all graphs of Fig. 5. These shear structures (minus contours) are probably caused by the impingement of shear layer onto the pipe wall.

When we compare the results obtained by LSE and QSE, we observe that LSE (Fig. 5(a) and (c)) and QSE (Fig. 5(b) and (d)) show similar results in general, particularly in relation to the large vortex structure on the right side of the wall mass transfer measurement sensor. However, when using the QSE, it can be seen that the intensities of the nondimensional shear and vortex structures are strengthened, which implies that a strong nonlinear relationship likely exists between the flow field and the wall mass transfer coefficient. When we compare the results for two different Schmidt numbers, we observe that the region formed by vortex structures (positive contours) downstream and upstream of the mass transfer measurement sensor and the region formed by shear structures (negative contours) just on the top of the mass transfer measurement sensor are quite similar. However, the positions of the vortex structures for the two Schmidt numbers are different, which may be due to the different Schmidt numbers. In this study, we only measured two Schmidt numbers, more cases are needed to get conclusive results.

The main research objective of the present study is to reveal the mechanisms of FAC. Therefore, we selected the positions of the cross sections based on the regions where FAC usually occurs. In our study, we found that the maximum mean wall mass transfer coefficient occurs in the recirculation region at $x/R \approx 2$ [11], therefore we carried out the simultaneous measurements in the cross section at $x/R = 2$. In order to prove the reproducibility of the flow structures obtained by stochastic estimation, we also analyzed the cross section at $x/R = 1.8$. On the other hand, other researchers found that the maximum mean wall mass transfer occurs in the region 2–4 R [10]. According to our previous study on the flow field [17], this region includes both the recirculation and reattachment regions in orifice flow. Therefore, we have also provided the results of the cross section at $x/R = 4$ in the reattachment region.

Figs. 6–8 show the nondimensional swirling, shear strength, and streamline patterns based on the LSE and QSE of $u_{xyi} | k > k_{large}$ at cross sections located at $x/R = 2, 1.8$, and 4, respectively. As mentioned earlier, stochastic estimation requires that the velocity components have a relationship with the wall mass transfer coefficient; therefore, we only analyze the flow field in the region $y/R < -0.5$ near the sensor of the wall mass transfer measurement. It is possible to clearly see two vortex structures on each side of the sensor of the wall mass transfer measurement in Figs. 6–8. In addition, the fluid flows toward the pipe wall, which enhances the mass transport of the reactant in the fluid to the pipe wall. It is possible to observe clearer counter-rotating vortex pairs using the QSE, as shown in Figs. 6(b), 7(b) and 8(b). Moreover, it should be pointed out that results in Figs. 6–8 were measured for working fluids with two different Schmidt numbers. Although the details of the vortex structures in Figs. 6–8 are different, all figures show that the counter-rotating vortex pairs are associated with large wall mass transfer coefficients. Therefore, it is reasonable to assume the conclusion that counter-rotating vortex pairs are associated with large wall mass transfer coefficient is valid for a large range of Schmidt numbers (at least between 1600 and 2770).

Note that the conditional flow structures are three-dimensional in reality. However, using the data measured by stereo-PIV measurements, we can only obtain the projection of these three-dimensional flow structures onto the laser sheet. It can be seen that the flow structures in Figs. 6–8 are not symmetric with respect to the pipe center. One possible reason is because the projection of the three-dimensional flow structures onto the laser sheet deviates from a symmetric pattern. Although it is extremely difficult to do the simultaneous measurement for sufficiently long time using high-speed cameras as we mentioned in the introduction, it probably will improve the symmetry of these conditional vortices shown in Figs. 6–8.

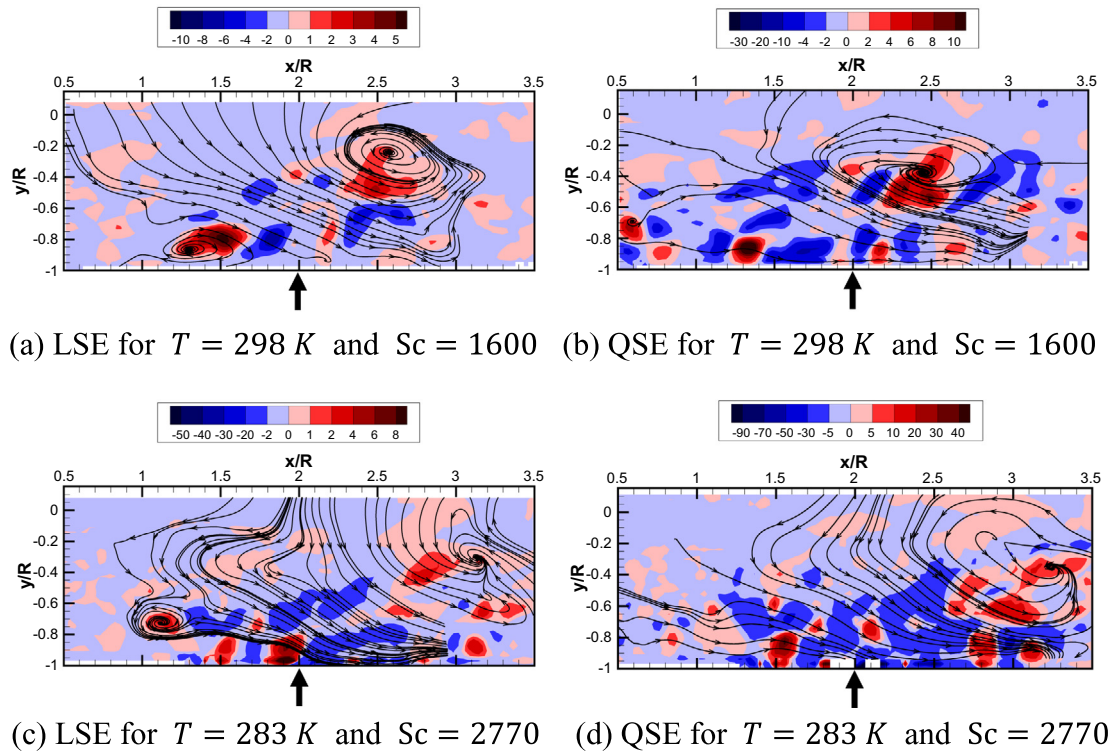


Fig. 5. Swirling, shear strength, and streamline patterns of the estimated fluctuating velocity field for $u_{xyi}|k > k_{large}$ at $x/R = 2$.

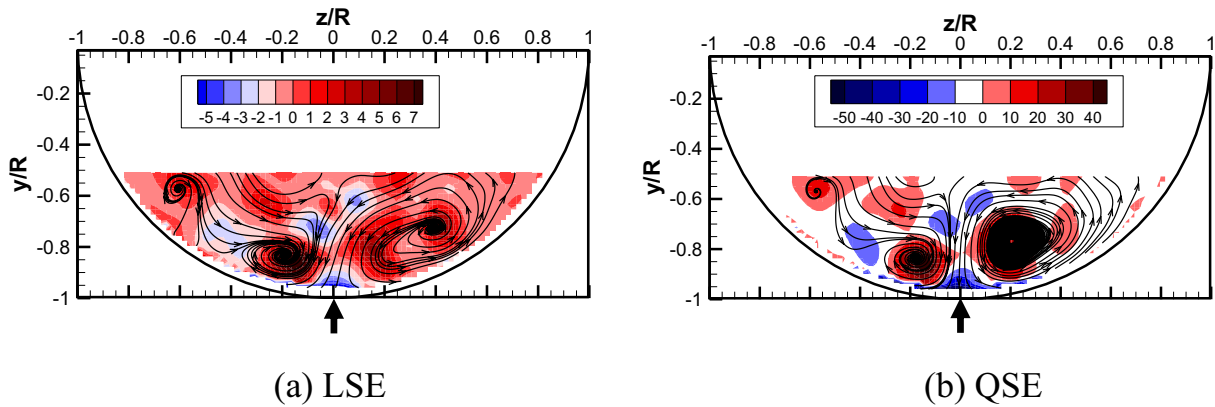


Fig. 6. Swirling, shear strength, and streamline patterns of the estimated fluctuating velocity field for $(u_{yzi}|k > k_{large})$ at $x/R = 2$ ($T = 298\text{ K}$, $Sc = 1600$).

As we mentioned in the introduction, the present study using the stochastic estimation is a continuation of our previous study using POD [11]. Therefore, it is meaningful to discuss the key differences between the methods and results of the two studies. It is widely known that POD analyzes the turbulent structures from the viewpoint of turbulent kinetic energy, which extracts the most energetic large-scale turbulent structures. However, the stochastic estimation calculates the turbulent structures satisfying specified conditions, which can be objectively determined by researchers. The previous study revealed that the second POD eigenmode in the recirculation region “compression and expansion mode” is probably the reason why the maximum mean wall mass transfer coefficient occurs at approximately one pipe diameter downstream from the orifice plate when the β ratio is 0.62. Additionally, our previous study reveals that there are relationship between the large-scale flow structures and the wall mass transfer coefficient.

However, we still do not know what these large-scale structures are. Moreover, it’s difficult to understand this kind of relationship from the contour plots of the spatio-temporal correlation of the flow field and the wall mass transfer coefficient.

The present study reveals that the counter-rotating vortex pairs are associated with large wall mass transfer coefficients. Additionally, from the equations used for the SE in Section 3, we know that the stochastic estimation calculates the conditional average flow field using unconditional correlation functions. Therefore, the stochastic estimation does not contain more information than the correlation functions, but it interprets the unconditional correlation functions so that they are much easier to understand. More specifically, the stochastic estimation offers an opportunity to interpret the correlation function by vector fields, from which it is easy to derive the streamline patterns, swirling, and shear strength, as shown in Figs. 5–8.

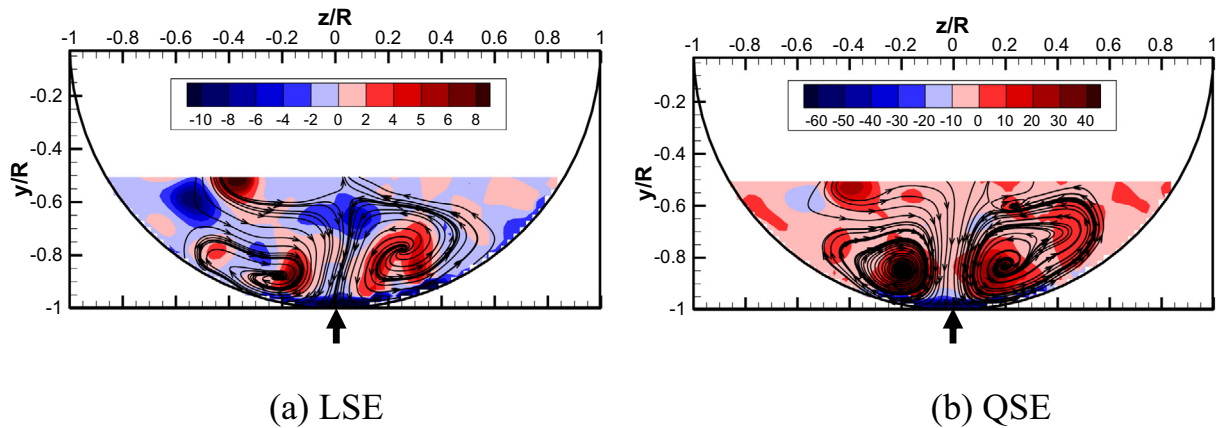


Fig. 7. Swirling, shear strength, and streamline patterns of the estimated fluctuating velocity field for $\langle u_{yzi} | k > k_{\text{large}} \rangle$ at $x/R = 1.8$ ($T = 283\text{ K}$, $Sc = 2770$).

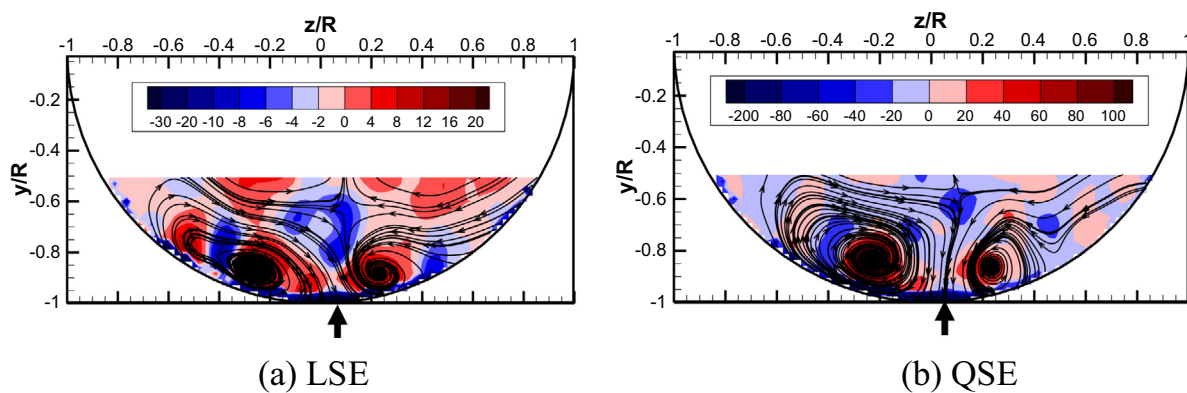
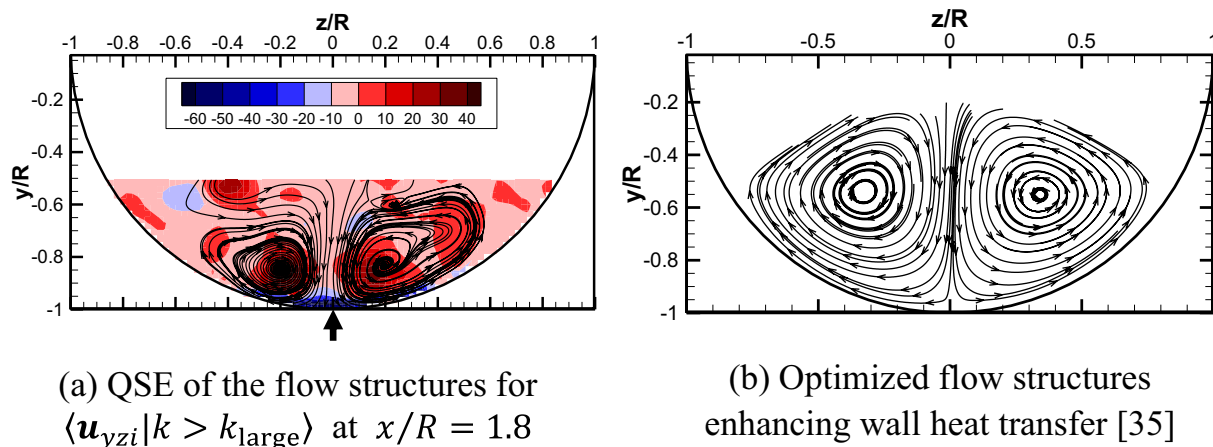


Fig. 8. Swirling, shear strength, and streamline patterns of the estimated fluctuating velocity field for $\langle u_{yzi} | k > k_{\text{large}} \rangle$ at $x/R = 4$ ($T = 283\text{ K}$, $Sc = 2770$).

It is also very interesting to note that similar vortex structures have been reported in theoretical and numerical studies regarding wall heat transfer enhancement [35]. Fig. 9 shows a comparison of flow structures that enhance wall mass transfer and wall heat transfer. The flow structure enhancing wall mass transfer is obtained on the basis of the QSE for $\langle u_{yzi} | k > k_{\text{large}} \rangle$ at $x/R = 1.8$. In contrast, the flow structure enhancing wall heat transfer is obtained by theoretically analyzing the irreversibility of the heat transfer process [35]. More specifically, the exergy destruction rate

was set as an optimization objective, and the fluid power consumption was set as a constraint condition. A momentum equation with an additional volume force was constructed through a functional variation to numerically simulate the convective heat transfer by coupling with an energy equation. The authors found that the longitudinal swirl flow with multiple vortexes is a flow pattern with good heat-transfer performance inside circular pipes. In order to compare the multivortex flow structures in [35] with the experimental results in the present study, only one vortex pair is shown



(a) QSE of the flow structures for $\langle u_{yzi} | k > k_{\text{large}} \rangle$ at $x/R = 1.8$

(b) Optimized flow structures enhancing wall heat transfer [35]

Fig. 9. Comparison of the flow structures enhancing wall mass transfer and wall heat transfer based on the exergy destruction optimization.

in Fig. 9(b). It is observed that a similar counter-rotating vortex pair is obtained by the theoretical optimization and numerical simulation. It is necessary to point out that the work in [35] was not conducted to validate the work in the present study; therefore, the hydrodynamic conditions in [35] as well as the physical properties of the working fluid are different from those in the present study. Therefore, the sizes of the counter-rotating vortex pairs are quite different between these two cases.

5. Conclusions

We used both linear and quadratic stochastic estimation methods to analyze the flow structures associated with the conditions of large wall mass transfer coefficients, the conditions of which were determined from the pdf and cdf of the fluctuations in the wall mass transfer coefficient. In the single-point stochastic estimation in the present study, the use of a quadratic term was shown to considerably increase the intensity of the vortex structures, which implies that the flow field has a nonlinear relationship with the wall mass transfer coefficient. The results for both longitudinal and cross sections suggest that vortex structures appear when a large wall mass transfer coefficient exists. The results from the cross-sectional measurements reveal that counter-rotating vortex pairs are associated with large wall mass transfer coefficients. Therefore, if it is possible to prevent the generation of such structures in the flow field, it should also be possible to suppress the mass-transfer coefficient and thus pipe-wall thinning problems. In addition, if the aim is to enhance the wall mass transfer coefficient, it is possible to control the flow field by generating more of these structures. Actually, similar vortex structures have been reported to enhance convective heat transfer from a theoretical analysis and numerical study in literature, which we believe is due to the analogy between heat and mass transfer.

Acknowledgements

The work was supported by the National Key Basic Research Program of China (973 Program) (2013CB228302) and the National Natural Science Foundation of China (51376069). In addition, we thank Prof. Ronald Adrian for the discussion of stochastic estimation by email. Finally, we thank Mr. Atsushi Fujishiro and Mr. Masashi Kano for their help with the experiment and Mr. Junbo Wang for providing the numerical data in Fig. 9(b).

References

- [1] T. Sydberger, U. Lotz, Relation between mass transfer and corrosion in a turbulent pipe flow, *J. Electrochem. Soc.* 129 (2) (1982) 276–283.
- [2] NISA, Secondary Piping Rupture Accident at Mihama Power Station, Unit 3, of the Kansai Electric Power Co. Inc., Final Report, 2005, 2005.
- [3] S. Chouikhi, M. Patrick, A. Wragg, Mass transfer downstream of nozzles in turbulent pipe flow with varying Schmidt number, *J. Appl. Electrochem.* 17 (6) (1987) 1118–1128.
- [4] T. Rizk, G. Thompson, J. Dawson, Mass transfer enhancement associated with sudden flow expansion, *Corros. Sci.* 38 (10) (1996) 1801–1814.
- [5] H. Togun, S. Kazi, A. Badarudin, A review of experimental study of turbulent heat transfer in separated flow, *Aust. J. Basic Appl. Sci.* 5 (10) (2011) 489–505.
- [6] W.H. Ahmed, M.M. Bello, M. El Nakla, A. Al Sarkhi, Flow and mass transfer downstream of an orifice under flow accelerated corrosion conditions, *Nucl. Eng. Des.* 252 (2012) 52–67.
- [7] M. El-Gammal, W.H. Ahmed, C.Y. Ching, Investigation of wall mass transfer characteristics downstream of an orifice, *Nucl. Eng. Des.* 242 (2012) 353–360.
- [8] Y. Hasegawa, N. Kasagi, Low-pass filtering effects of viscous sublayer on high Schmidt number mass transfer close to a solid wall, *Int. J. Heat Fluid Flow* 30 (3) (2009) 525–533.
- [9] J. Xiong, S. Koshizuka, M. Sakai, Turbulence modeling for mass transfer enhancement by separation and reattachment with two-equation eddy-viscosity models, *Nucl. Eng. Des.* 241 (8) (2011) 3190–3200.
- [10] T. Yamagata, A. Ito, Y. Sato, N. Fujisawa, Experimental and numerical studies on mass transfer characteristics behind an orifice in a circular pipe for application to pipe-wall thinning, *Exp. Therm. Fluid Sci.* 52 (2014) 239–247.
- [11] F. Shan, A. Fujishiro, T. Tsuneyoshi, Y. Tsuji, Effects of flow field on the wall mass transfer rate behind a circular orifice in a round pipe, *Int. J. Heat Mass Transfer* 73 (2014) 542–550.
- [12] Y. Utanohara, Y. Nagaya, A. Nakamura, M. Murase, Influence of local flow field on flow accelerated corrosion downstream from an orifice, *J. Power Energy Syst.* 6 (1) (2012) 18–33.
- [13] T. Takano, T. Yamagata, A. Ito, N. Fujisawa, Mass transfer measurements behind an orifice in a circular pipe flow for various combinations of swirl intensity and orifice bias, *J. Power Energy Syst.* 6 (2012) 402–411.
- [14] N. Fujisawa, T. Yamagata, S. Kanno, A. Ito, T. Takano, The mechanism of asymmetric pipe-wall thinning behind an orifice by combined effect of swirling flow and orifice bias, *Nucl. Eng. Des.* 252 (2012) 19–26.
- [15] T. Takano, Y. Ikarashi, K. Uchiyama, T. Yamagata, N. Fujisawa, Influence of swirling flow on mass and momentum transfer downstream of a pipe with elbow and orifice, *Int. J. Heat Mass Transfer* 92 (2016) 394–402.
- [16] N. Fujisawa, R. Watanabe, T. Yamagata, N. Kanatani, Characterization of pipe-flow turbulence and mass transfer in a curved swirling flow behind an orifice, in: *Progress in Wall Turbulence 2*, Springer, 2016, pp. 225–235.
- [17] F. Shan, A. Fujishiro, T. Tsuneyoshi, Y. Tsuji, Particle image velocimetry measurements of flow field behind a circular square-edged orifice in a round pipe, *Exp. Fluids* 54 (6) (2013) 1–18.
- [18] R.J. Adrian, J. Westerweel, *Particle Image Velocimetry*, Cambridge University Press, 2011.
- [19] R.J. Adrian, On the role of conditional averages in turbulence theory, in: *Turbulence in Liquids*, 1977, pp. 323–332.
- [20] L.M. Hudy, A. Naguib, W.M. Humphreys, Stochastic estimation of a separated-flow field using wall-pressure-array measurements, *Phys. Fluids* (1994–present) 19 (2) (2007).
- [21] N.E. Murray, L.S. Ukeiley, Estimation of the flowfield from surface pressure measurements in an open cavity, *AIAA J.* 41 (5) (2003) 969–972.
- [22] A.M. Naguib, C.E. Wark, O. Juckenhöfel, Stochastic estimation and flow sources associated with surface pressure events in a turbulent boundary layer, *Phys. Fluids* (1994–present) 13 (9) (2001) 2611–2626.
- [23] R.J. Adrian, Stochastic estimation of conditional structure: a review, *Appl. Sci. Res.* 53 (3–4) (1994) 291–303.
- [24] L. Sanchez-Caldera, *The Mechanism of Corrosion–Erosion in Steam Extraction Lines of Power Station*, Massachusetts Institute of Technology, Cambridge, Massachusetts, 1984.
- [25] C. Tropea, A.L. Yarin, J.F. Foss, *Springer Handbook of Experimental Fluid Mechanics*, Springer, 2007.
- [26] Y. Guezennec, Stochastic estimation of coherent structures in turbulent boundary layers, *Phys. Fluids A* (1989–1993) 1 (6) (1989) 1054–1060.
- [27] N. Murray, L. Ukeiley, Estimating the Shear Layer Velocity Field above an Open Cavity from Surface Pressure Measurements, *AIAA Paper* 2002–2866, 2002.
- [28] J.S. Son, T.J. Hanratty, Limiting relation for the eddy diffusivity close to a wall, *AIChE J.* 13 (4) (1967) 689–696.
- [29] A. Sciacchitano, D.R. Neal, B.L. Smith, S.O. Warner, P.P. Vlachos, B. Wieneke, F. Scarano, Collaborative framework for PIV uncertainty quantification: comparative assessment of methods, *Meas. Sci. Technol.* 26 (7) (2015) 074004.
- [30] D.R. Neal, A. Sciacchitano, B.L. Smith, F. Scarano, Collaborative framework for PIV uncertainty quantification: the experimental database, *Meas. Sci. Technol.* 26 (7) (2015) 074003.
- [31] K. Christensen, F. Scarano, Uncertainty quantification in particle image velocimetry, *Meas. Sci. Technol.* 26 (7) (2015) 070201.
- [32] B. Wieneke, PIV uncertainty quantification from correlation statistics, *Meas. Sci. Technol.* 26 (7) (2015) 074002.
- [33] R. Adrian, Stochastic estimation of conditional structure, in: J.P. Bonnet, M.N. Glauser (Eds.), *Eddy Structure Identification in Free Turbulent Shear Flows*, Springer, Netherlands, 1993, pp. 271–280.
- [34] R. Adrian, K. Christensen, Z.-C. Liu, Analysis and interpretation of instantaneous turbulent velocity fields, *Exp. Fluids* 29 (3) (2000) 275–290.
- [35] J. Wang, W. Liu, Z. Liu, The application of exergy destruction minimization in convective heat transfer optimization, *Appl. Therm. Eng.* 88 (2015) 384–390.